ChemComm

COMMUNICATION

View Article Online
View Journal | View Issue

Cite this: *Chem. Commun.*, 2026, 62, 8188

Received 6th January 2026,
Accepted 17th March 2026

DOI: 10.1039/d5cc07291c

rsc.li/chemcomm

Dual-temperature photothermal tandem catalysis for CO_2 conversion to olefins

Ziyang Li,[a] Yuhang Qi, *[a] Lipu Han,[a] Chu Zhang,[a] Zhenwen Yang,[a] Zhike Wu[a] and Shanshan Xu *[bc]

We report a dual-temperature photothermal tandem system that overcomes temperature mismatch for CO_2 hydrogenation to light olefins in a single reactor. A graphene-modified In_2O_3 top bed enables higher-temperature RWGS, and a K-doped Fe_2O_3 bottom bed facilitates lower-temperature FTS. This vertical configuration couples the two reactions, achieving a light-olefin production rate of 52.1 μmol g^{-1} h^{-1} with 69% selectivity at 0.05 MPa without external heating.

The increasing atmospheric CO_2 level is aggravating climate change and energy insecurity, highlighting the urgent need for sustainable carbon-recycling technologies.[1,2] Among the various strategies, photothermal CO_2 reduction has attracted growing attention because it does not require external electrical input and enables full-spectrum solar utilization to activate inert CO_2 molecules.[3,4] Significant progress has been achieved in CO_2 hydrogenation to C_1 products such as CH_4, CO, and CH_3OH.[5,6] However, overcoming the kinetic barriers associated with C–C bond formation to directly produce C_2^+ hydrocarbons remains highly challenging.[7,8]

For thermocatalytic CO_2 hydrogenation towards C_2^+ products, two tandem strategies are most frequently explored. One approach involves coupling CO_2-to-methanol with a subsequent methanol-to-olefins (MTO) process.[9,10] Although this route can yield light olefins, methanol selectivity is highly pressure-dependent. It typically requires elevated pressures to suppress methanol decomposition, which is unfavourable for scalable operations under photothermal conditions. Another widely studied route converts CO_2 to CO *via* the reverse water–gas shift (RWGS) reaction, followed by Fischer–Tropsch synthesis (FTS) to form hydrocarbons.[11–13] Integrating RWGS and FTS in a single reactor is intrinsically difficult because the two steps require different optimal temperature windows: RWGS is endothermic and favours high temperatures >400 °C for efficient CO formation,[14,15] whereas FTS requires moderate temperatures (200–350 °C) to promote C–C coupling and avoid excessive methane formation.[16,17] This fundamental temperature mismatch is a key limitation to achieving direct CO_2-to-olefin conversion in a single photothermal reactor.

Compared with the recently reported single-reactor tandem photothermal system,[18] this work employs a dual-bed reactor in which the RWGS and FTS functions are spatially separated. This design enables cascade heat utilization, suppresses local overheating, and allows independent optimization of each catalytic bed for improved flexibility in tuning target products. The top layer, made of graphene-modified In_2O_3 (G–In_2O_3), exhibits excellent photothermal conversion and efficiently reduces CO_2 to CO while simultaneously heating the gas phase and transferring heat to the downstream bed *via* combined radiative and convective heat transfer. This controlled heat flow determines the lower temperature of the potassium-doped Fe_2O_3 (K–Fe_2O_3) bed, where CO undergoes FTS to produce light olefins with high selectivity. The vertically stacked configuration establishes a well-defined temperature gradient, enabling the RWGS and FTS stages to operate within their respective optimal temperature ranges. Under low pressure (0.05 MPa), the tandem system achieves a light-olefin production rate of 52.1 μmol g^{-1} h^{-1} with 69% selectivity, demonstrating that engineering a temperature gradient is an effective strategy to overcome the inherent temperature mismatch in tandem photothermal catalysis.

The G–In_2O_3 composite in the top bed was prepared by using the hydrothermal method. The average particle size of In_2O_3 particles is 50–100 nm, and they are uniformly dispersed on the graphene sheets (Fig. S1). The high-resolution transmission electron microscopy (HRTEM) image (Fig. 1a) shows a distinct interface between graphene and In_2O_3. The corresponding fast Fourier transform patterns provide atomic-resolution structural information: the cubic lattice spots can be assigned to In_2O_3, while the hexagonal pattern arises from the characteristic six-fold

[a] *School of Electronics and Information Engineering, Hebei University of Technology, Tianjin 300130, China. E-mail: yuhangqi@hebut.edu.cn*
[b] *Department of Materials, School of Natural Science, The University of Manchester, Oxford Road, Manchester M13 9PL, UK. E-mail: shanshan.xu@manchester.ac.uk*
[c] *University of Manchester at Harwell, Harwell Science and Innovation Campus, Didcot, Oxfordshire OX11 0DE, UK*

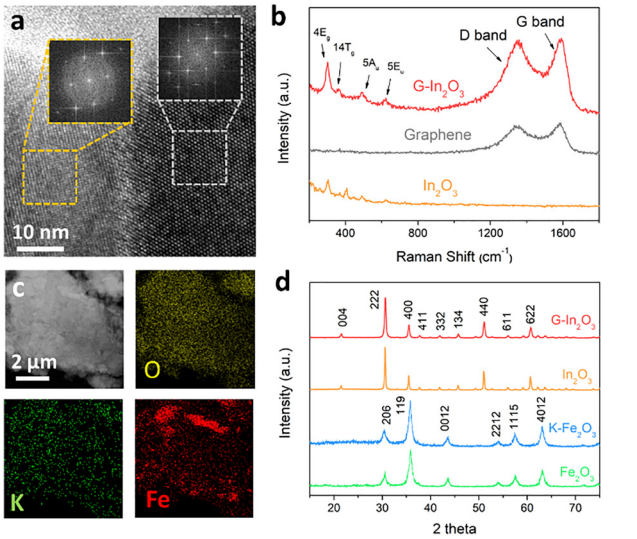

Fig. 1 (a) The HRTEM image of G–In_2O_3-10% and the corresponding fast Fourier transform, (b) the Raman spectra of graphene, In_2O_3 and G–In_2O_3-10%, (c) the elemental mapping of K–Fe_2O_3-5%, and (d) the XRD patterns of In_2O_3, G–In_2O_3-10%, Fe_2O_3 and K–Fe_2O_3-5%.

symmetry of graphene. Raman spectroscopy further confirms the formation of the G–In_2O_3 composite (Fig. 1b). The D band at $\sim$1300 cm^{-1} and the G band at $\sim$1400 cm^{-1} are characteristic of graphene, whereas the peaks at 307, 366, 494, and 628 cm^{-1} are aligned with the In–O vibrations of InO_6 structural units in the body-centred cubic In_2O_3 structure.

Potassium modification of Fe_2O_3 in the lower catalyst bed was verified by SEM and elemental mapping, which shows that K is homogeneously distributed on Fe_2O_3 (Fig. 1c). TEM and HRTEM analyses indicate that the lattice spacings of K–Fe_2O_3 are 0.251, 0.208, and 0.295 nm, corresponding to the (311), (400), and (220) crystal planes of γ-Fe_2O_3 (Fig. S2). As shown in the X-ray diffraction (XRD) patterns (Fig. 1d), all diffraction peaks can be indexed to Fe_2O_3 (JCPDS No. 39-1346) and In_2O_3 (JCPDS No. 71-2194),[19,20] indicating that the crystalline structures of both oxides are preserved after graphene and K modification.

In the catalyst selection for this dual-bed reactor, In_2O_3 was chosen because it is an efficient catalyst for the RWGS reaction and can produce CO with nearly 100% selectivity. The generated CO acts as the substrate for the FTS reaction, thereby initiating the tandem reaction. Fe_2O_3 was selected instead of Fe_5C_2 because it offers advantages such as facile preparation, low cost, and good structural stability. In addition, Fe_2O_3 can be transformed into the active Fe_5C_2 phase through *in situ* phase conversion under reaction conditions.

To determine the optimal composition for CO_2 conversion, we evaluated G–In_2O_3 composites with various graphene loadings in the photothermal RWGS reaction (Fig. S3) and K-modified Fe_2O_3 with different K contents in FTS (Fig. S4). As shown in Fig. S5, all the G–In_2O_3 composites produce CO as the only product, confirming that graphene incorporation does not alter the reaction pathway. The CO production rate increases progressively, reaching a maximum for G–In_2O_3-10%, but drops when the loading is further increased to 15 wt%. At moderate loadings ($<$10 wt%), graphene improves the dispersion of In_2O_3 and its specific surface area (Fig. S6) and enhances CO_2 adsorption and activation (Fig. S7).[21] The strong broadband absorption of graphene raises the catalyst surface temperature under illumination, thereby accelerating the endothermic RWGS reaction (Fig. S8).[22] Graphene also suppresses non-radiative recombination of photogenerated carriers in In_2O_3, resulting in a higher photothermal conversion efficiency (Fig. S9).[23,24] Such effects contribute to the enhanced CO production at the optimal 10 wt% loading. However, excessive graphene loadings will block In_2O_3 active sites and reduce the accessible surface area for gas adsorption, leading to reduced CO production.

In the following FTS reaction, introducing potassium significantly changes both hydrocarbon distribution and light-olefin productivity. As shown in Fig. S10, the K–Fe_2O_3 catalyst containing 2.5 wt% K exhibits the highest light-olefin production rate (*i.e.*, 0.55 mmol g^{-1} h^{-1} for C_2H_4 and 0.37 mmol g^{-1} h^{-1} for C_3H_6). In contrast, although the overall olefin production rate declines at higher K loadings, the K–Fe_2O_3 with 5 wt% K catalyst shows the highest selectivity toward $C_{2-3}^{=}$ olefins (51%), accompanied by a suppressed formation of CH_4. A moderate amount of potassium improves the catalytic performance by slightly reducing the photoluminescence intensity of Fe_2O_3 (Fig. S11) and enhancing CO adsorption and activation (Fig. S12). However, excessive K loading further neutralises surface acidity and suppresses H_2 chemisorption, thus lowering the FTS reaction rate and shifting the product distribution away from CH_4 and toward heavier hydrocarbons and a higher olefin fraction, which agrees with the trends in Fig. S10.[25,26] Furthermore, the photothermal FTS performance of K–Fe_2O_3 was evaluated under identical conditions while varying the light intensity, as detailed in Fig. S13.

After optimising the compositions of G–In_2O_3 and K–Fe_2O_3, we evaluated tandem photothermal CO_2 hydrogenation over the G–In_2O_3-10% and K–Fe_2O_3-5% catalyst. The hydrocarbon selectivity and product distribution depend strongly on the integration configuration of the two components. The single K–Fe_2O_3 component shows low activity and poor olefin selectivity (*i.e.*, 50%) because it cannot accumulate sufficiently high CO concentrations, allowing the Sabatier reaction to proceed and producing CH_4 (*i.e.*, 48%) as the product (Fig. 2a and Fig. S14). In contrast, single In_2O_3 primarily generates CO as a product with negligible hydrocarbons, as the low-pressure and high-temperature conditions are unfavourable for methanol or olefin formation. Simply mixing two components physically (granule stacking) shows only a minor tandem effect, indicating that excessive proximity does not enable optimal photothermal CO_2-to-olefin performance.

Therefore, we adopt a dual-bed configuration, with G–In_2O_3-10% in the upper layer and K–Fe_2O_3-5% in the lower layer, separated by an inert screen (Fig. 2a). When K–Fe_2O_3-5% is positioned beneath G–In_2O_3-10%, the light-olefin production rate achieved was 52.1 μmol g^{-1} h^{-1} with a selectivity of 69%. In contrast, reversing the order—placing K–Fe_2O_3-5% above G–In_2O_3-10%—resulted in a significantly lower olefin productivity,

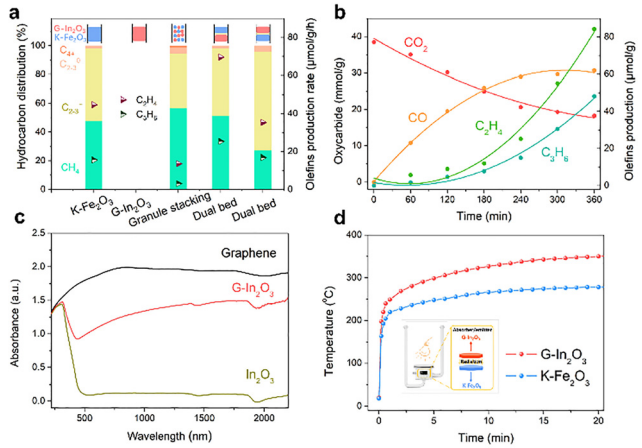

Fig. 2 (a) Effect of the integration mode of G–In_2O_3-10% and K–Fe_2O_3-5% (mass ratio 3 : 5) on hydrocarbon distribution and light-olefin production rate under identical photothermal CO_2 hydrogenation conditions. (b) Time profiles of CO_2, CO, C_2H_4 and C_3H_6 over the dual-bed G–In_2O_3-10%/K–Fe_2O_3-5% catalyst under continuous illumination. (c) The UV-Vis-NIR spectra of graphene, In_2O_3 and G–In_2O_3-10%. (d) Time evolution of the surface temperature of the G–In_2O_3-10% and K–Fe_2O_3-5% beds.

confirming that efficient tandem CO_2 reduction and F–T coupling require the correct thermal and reactant-flow sequence. This improvement arises from the temperature distribution and reaction dynamics revealed in Fig. 2b. In the dual-bed configuration, the upper G–In_2O_3-10% layer, operating at a higher photothermal temperature, rapidly converts CO_2 to CO and steadily increases the CO concentration throughout the reaction (Fig. 2b). As CO continues to accumulate, the concentration surpasses the threshold required to trigger chain-growth reactions in the downstream FTS bed. Olefin production begins to rise significantly after 120 min and continues to increase over time. Meanwhile, the CO formation rate gradually approaches a quasi-steady state, while CO_2 is continuously consumed. These results demonstrate that the upper G–In_2O_3 bed must supply CO with high selectivity and rate to initiate and sustain FTS in the lower K–Fe_2O_3 bed, thereby enabling efficient tandem photothermal CO_2-to-olefin conversion. Detailed analysis of the stability test is provided in Fig. S15 of the SI.

As a result, the photothermal conversion efficiency of the upper G–In_2O_3 layer is crucial. The light source primarily irradiates the top bed containing G–In_2O_3. G–In_2O_3 was selected because the tandem process is initiated by light-driven RWGS, which produces CO as the key intermediate for the subsequent FTS reaction in the lower bed. Positioning In_2O_3 in the upper bed promotes the formation of a CO-rich stream under continuous unidirectional gas flow. Moreover, UV-Vis-NIR spectra (Fig. 2c) show that pristine In_2O_3, as a wide-band-gap semiconductor (3.2 eV, Fig. S16), shows weak absorption across visible and near-infrared regions. Graphene endows G–In_2O_3 with strong, nearly broadband light absorption, enabling efficient photothermal conversion. The heat generated in the upper bed can also be transferred to the downstream K–Fe_2O_3 bed through thermal radiation and gas-phase convection, helping to maintain the temperature required for the tandem reaction. The resulting thermal distribution in the dual-bed configuration is confirmed under photothermal operation (Fig. 2d): the upper G–In_2O_3 layer rapidly reaches ~360 °C within 10 min, while the lower K–Fe_2O_3 layer stabilises at ~260 °C. The respective temperatures also precisely correspond to the optimal adsorption range (Fig. S17).[27]

To identify the active sites in G–In_2O_3 for CO_2 reduction, XPS and EPR measurements were carried out. In comparison, the corresponding peaks of G–In_2O_3 shift to lower binding energies, which can be attributed to electron transfer at the graphene/In_2O_3 interface and an increased concentration of oxygen vacancies (Fig. 3a). The O 1s spectra (Fig. 3b) can be deconvoluted into two contributions: the peak at 529.8 eV is assigned to lattice oxygen in In–O–In, whereas the peak at 531.4 eV is associated with oxygen vacancies.[28] Furthermore, the stronger EPR signal for G–In_2O_3 shows that it has a higher oxygen-vacancy level (Fig. 3c),[29] aligning with the XPS results. This suggested that carbon at the graphene/In_2O_3 interface lowers the energy needed to create oxygen vacancies in the In_2O_3 lattice.

Because the oxygen vacancy concentration evolves under photothermal reaction conditions, we compared the XRD, PL, EPR and UV-vis-NIR spectra of G–In_2O_3 before and after the reaction (Fig. S18–S21). Detailed characterization and analysis are provided in the SI.

Regarding the active phase of the K–Fe_2O_3 catalyst in the FTS reaction, XPS measurements were carried out to determine the surface elemental composition and chemical states (Fig. 3d). In the Fe 2p spectrum, upon K promotion, the Fe $2p_{3/2}$ peak shifts to a lower binding energy, indicating a more reduced Fe environment and thus facilitating the transformation of Fe species into Fe_5C_2, which is widely recognised as the active phase for FTS in Fe-based catalysts.[30–32] In the C 1s spectrum (Fig. 3e), three C 1s components together with an additional K 2p signal are observed. Compared with pristine Fe_2O_3, the K–Fe_2O_3 sample

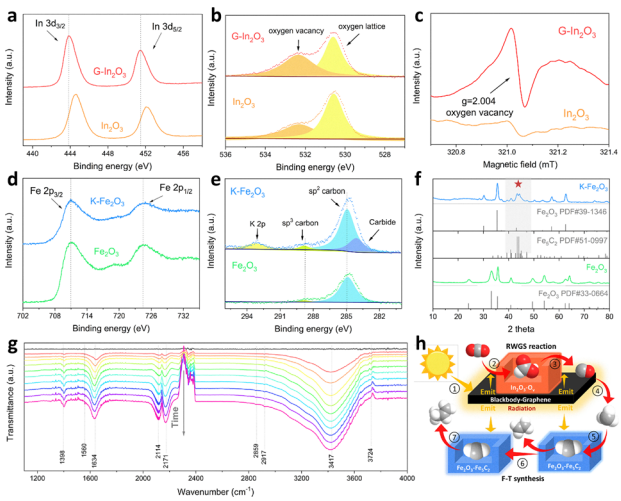

Fig. 3 The XPS spectra of (a) In 3d and (b) O 1s, (c) the EPR spectra of G–In_2O_3-10% and In_2O_3, the XPS spectra of (d) Fe 2p and (e) C 1s, (f) the XRD patterns of K–Fe_2O_3-5% and Fe_2O_3, (g) the *in situ* FTIR spectra of G–In_2O_3-10% and K–Fe_2O_3-5%, and (h) the advance and process of the photothermal CO_2 reduction to light olefins.

exhibits new carbide-related C 1s features, aligning with the leftward shift of the Fe $2p_{3/2}$ peak.[33] XRD patterns of Fe_2O_3 and K–Fe_2O_3 (Fig. 3f) further reveal that additional reflections in K–Fe_2O_3 can be indexed to the main diffraction peaks of Fe_5C_2, with no Fe_3C phase detected (Fig. S22).[34,35] K doping plays multiple roles in the Fe-based catalyst by enhancing CO adsorption and activation, increasing chain-growth probability, and suppressing the secondary hydrogenation of olefins, thereby improving light-olefin selectivity. In addition, K facilitates the formation and stabilization of the Fe_5C_2 active phase, which contributes to the enhanced FTS performance.[36]

Although In_2O_3 is widely recognized as an effective catalyst for CO_2 hydrogenation to methanol under relatively high pressures, the reaction in this work was performed at 0.5 atm, which is less favorable for methanol formation.[37] To elucidate the CO_2 activation pathway, *in situ* FTIR spectroscopy was conducted (Fig. 3g). The spectra show a band at 1398 cm^{-1} assigned to carbonate species and a band at 1560 cm^{-1} attributed to COOH* intermediates. Since COOH* species are generally associated with the RWGS pathway to CO rather than the methanol pathway *via* HCOO*, these results indicate that CO is the predominant product in the present system. The feature at 1634 cm^{-1} originates from adsorbed water, and the bands at 2114 and 2171 cm^{-1} are ascribed to linearly and bridge-bonded adsorbed CO*, respectively. The band at 2917 cm^{-1} is characteristic of CH_3* species, and the broad absorptions at 3417 and 3724 cm^{-1} are associated with surface hydroxyl groups and adsorbed water molecules.[38] Accordingly, these surface intermediates provide direct spectroscopic evidence for a tandem RWGS–FTS mechanism, wherein CO_2 is first reduced to CO *via* RWGS, and then the resulting CO is subsequently hydrogenated through CH_x* intermediates to form light hydrocarbons.[39–41]

In summary, we have developed a tandem dual-temperature catalytic configuration that enables controlled multi-stage temperature distribution and efficient energy utilisation for the photothermal hydrogenation of CO_2 into high-value hydrocarbons. In the upper bed, G–In_2O_3 drives the RWGS reaction. The absorbed light energy is converted into heat and transmitted to the underlying K–Fe_2O_3 bed *via* both radiative and convective heat transfer. In the lower bed, K–Fe_2O_3 drives the FTS process (Fig. 3h). By synergistically engineering the dual-bed catalysts with optimal operational temperatures in a single photothermal reactor, we achieve direct CO_2-to-light-olefin conversion with a production rate of 52.1 μmol g^{-1} h^{-1} and a selectivity of 69%, demonstrating a promising strategy for solar-driven CO_2 valorisation.

Z. L.: Investigation, Methodology, Writing – original draft. L. H. and C. Z.: Formal analysis, Data curation. Z. Y. and Z. W.: Investigation, Validation, Visualization. Y. Q.: Conceptualization, Supervision, Project administration. S. X.: Conceptualization, Writing – review & editing.

Conflicts of interest

There are no conflicts to declare.

Data availability

Data will be made available on request. Supplementary information is available. See DOI: https://doi.org/10.1039/d5cc07291c.

Acknowledgements

The authors appreciate the support from the National Natural Science Foundation of China (52402246) and the Natural Science Foundation of Hebei (E2023202267). S. X. acknowledges the start-up funding from the University of Manchester and the University of Manchester Harwell Campus.

References

1 F. Xu, F. Zhao, X. Deng, J. Zhang, J. Zhang, C. Ai, J. Yu and H. García, *Nat. Commun.*, 2025, **16**, 6882.
2 X. Wan, Y. Li, Y. Chen, J. Ma, Y.-A. Liu, E.-D. Zhao, Y. Gu, Y. Zhao, Y. Cui, R. Li, D. Liu, R. Long, K. M. Liew and Y. Xiong, *Nat. Commun.*, 2024, **15**, 1273.
3 Z. Xiao, L. Zhang, X. Tan, K. Sun, J. Li, L. Pan, J. J. Zou, G. Li and D. Wang, *Adv. Funct. Mater.*, 2025, **35**, 2500339.
4 X. Ding, W. Liu, J. Zhao, L. Wang and Z. Zou, *Adv. Mater.*, 2025, **37**, 2312093.
5 W. Gao, Y. Li, D. Xiao and D. Ma, *J. Energy Chem.*, 2023, **83**, 62–78.
6 S. Khan, X. Dai, T. Ali, S. Mahmood, M. U. Haq, M. S. Riaz and Y. Hu, *Int. J. Hydrogen Energy*, 2023, **48**, 24756–24787.
7 E. Ø. Pedersen, I.-H. Svenum and E. A. Blekkan, *J. Catal.*, 2018, **361**, 23–32.
8 Z. Li, L. Zhong, F. Yu, Y. An, Y. Dai, Y. Yang, T. Lin, S. Li, H. Wang, P. Gao, Y. Sun and M. He, *ACS Catal.*, 2017, **7**, 3622–3631.
9 S. Garg, Z. Xie and J. G. Chen, *Nat. Chem. Eng.*, 2024, **1**, 139–148.
10 L. Wang, Y. Sun, F. Zhang, J. Hu, W. Hu, S. Xie, Y. Wang, J. Feng, Y. Li, G. Wang, B. Zhang, H. Wang, Q. Zhang and Y. Wang, *Adv. Mater.*, 2023, **35**, 2205782.
11 S. Ning, H. Ou, Y. Li, C. Lv, S. Wang, D. Wang and J. Ye, *Angew. Chem., Int. Ed.*, 2023, **62**, e202302253.
12 H. Song, K. Sun, H. Huang, S. Ning, S. Wang, Z. Wang, Y. Weng, Y. Cui, Y. Li, X.-S. Wang, D. Wang, L. Liu, Z.-J. Wang and J. Ye, *Nat. Commun.*, 2025, **16**, 2831.
13 R. Li, Y. Li, Z. Li, S. Ouyang, H. Yuan and T. Zhang, *Adv. Mater.*, 2023, **35**, e2307217.
14 S. Mo, S. Li, J. Zhou, X. Zhao, H. Zhao, X. Zhou, Y. Fan, Z. Zhu, B. Li, Q. Xie, W. Si, Y. Chen, D. Ye and J. Li, *ACS Catal.*, 2025, **15**, 2796–2808.
15 L. Wang, Y. Dong, T. Yan, Z. Hu, F. M. Ali, D. M. Meira, P. N. Duchesne, J. Y. Y. Loh, C. Qiu, E. E. Storey, Y. Xu, W. Sun, M. Ghoussoub, N. P. Kherani, A. S. Helmy and G. A. Ozin, *Nat. Commun.*, 2020, **11**, 2432.
16 Z. Xie, X.-Y. Yu, Z. Zhang, X. Wang and T. Xie, *ACS Appl. Mater. Interfaces*, 2025, **17**, 19617–19628.
17 Q. Hao, Z. Li, Y. Shi, R. Li, Y. Li, S. Ouyang, H. Yuan and T. Zhang, *Nano Energy*, 2022, **102**, 107723.
18 S. Ning, X. Wu, H. Song, X. Ma, S. Yue, S. Zhang, L. Tang, R. Liu, X. Yin, S. Ouyang and J. Ye, *J. Am. Chem. Soc.*, 2025, **148**, 1728–1740.
19 P. Cao, X. Xu, F. Jia, Y. Zeng, W. Liu, C. Wang, S. Han, M. Fang, X. Liu, D. Zhu and S. T. Navale, *Appl. Surf. Sci.*, 2025, **688**, 162424.
20 C.-Q. Guo, H.-S. Zheng, J. Yang, X. Xiang and Z.-Y. Zhao, *Appl. Surf. Sci.*, 2025, **685**, 162063.
21 F. Hu, X. Chen, Z. Tu, Z.-H. Lu, G. Feng and R. Zhang, *Ind. Eng. Chem. Res.*, 2021, **60**, 12235–12243.
22 Z. Zhang and Z. Zhu, *Appl. Surf. Sci.*, 2022, **601**, 154243.
23 X. Jin, Q. Guan, T. Tian, H. Li, Y. Han, F. Hao, Y. Cui, W. Li, Y. Zhu and Y. Zhang, *Appl. Surf. Sci.*, 2020, **504**, 144241.
24 M. A. M. Khan, R. Siwach, S. Kumar, J. Ahmed and M. Ahamed, *J. Alloys Compd.*, 2020, **846**, 156479.
25 J. Huang, G. Zhang, M. Wang, J. Zhu, F. Ding, C. Song and X. Guo, *Front. Energy Res.*, 2023, **10**, 995800.
26 H. Zhang, H. Ma, H. Zhang, W. Ying and D. Fang, *Catal. Lett.*, 2011, **142**, 131–137.

27 P. Bredy, D. Farrusseng, Y. Schuurman and F. C. Meunier, *J. Catal.*, 2022, **411**, 93–96.
28 C. Shen, K. Sun, R. Zou, Q. Wu, D. Mei and C.-J. Liu, *Appl. Catal., B*, 2025, **361**, 124683.
29 X. Yu, Y. Chen, Q. Zhang, Y. Yin, D. Sun, Y. Ru and G. Tian, *Surf. Interfaces*, 2023, **38**, 102789.
30 L. Song, S. Ouyang, P. Li and J. Ye, *J. Mater. Chem. A*, 2022, **10**, 16243–16248.
31 Z. Zhang, B. Chen, L. Jia, W. Liu, X. Gao, J. Gao, B. Meng, Y. Tan, Y. He, W. Tu and Y.-F. Han, *Appl. Catal., B*, 2023, **327**, 122449.
32 H. Wang, X. Nie, Y. Liu, M. J. Janik, X. Han, Y. Deng, W. Hu, C. Song and X. Guo, *ACS Appl. Mater. Interfaces*, 2022, **14**, 37637–37651.
33 M. A. Hoque, M. I. Guzman, J. P. Selegue and M. K. Gnanamani, *Materials*, 2022, **15**, 7378.
34 S. Najari, S. Saeidi, A. Sápi, Á. Szamosvölgyi, Á. Papp, A. Efremova, H. Bali and Z. Kónya, *Chem. Eng. J.*, 2024, **485**, 149787.
35 Y. Liu, Y. Ye, Y. Li, H. Du, Z. Yin, M. Li, Z. Huang, X. Zheng, H. Wang, Y. Wang and Y. Deng, *Mol. Catal.*, 2024, **556**, 113947.
36 L. Niu, X. Liu, X. Wen, Y. Yang, J. Xu and Y. Li, *Catal. Today*, 2020, **343**, 101–111.
37 J. Ye, C. Liu, D. Mei and Q. Ge, *ACS Catal.*, 2013, **3**, 1296–1306.
38 T. Yan, L. Wang, Y. Liang, M. Makaremi, T. E. Wood, Y. Dai, B. Huang, F. M. Ali, Y. Dong and G. A. Ozin, *Nat. Commun.*, 2019, **10**, 2521.
39 M. Zhang, J. Ren and Y. Yu, *ACS Catal.*, 2019, **10**, 689–701.
40 R. Li, Y. Li, Z. Li, W. Wei, Q. Hao, Y. Shi, S. Ouyang, H. Yuan and T. Zhang, *ACS Catal.*, 2022, **12**, 5316–5326.
41 J. Han, W. Liu, L. Zhang, H. Ren, C. Wu, J. Zhang, C. Gong, G. Yang, H. Yang, S. Zhang, H. Wang, T. Ji, J. Li and P. Gao, *ACS Catal.*, 2025, **15**, 3940–3954.